Liquid Crystals
Publication details, including instructions for authors and subscription information:
http://www.informaworld.com/smpp/title~content=t713926090

Streamline Image Analysis: a new tool for investigating defects in nematic liquid crystals

A. Sparavigna; A. Sanna; B. Montrucchio; A. Strigazzi

Online publication date: 06 August 2010

To cite this Article Sparavigna, A. , Sanna, A. , Montrucchio, B. and Strigazzi, A.(1999) 'Streamline Image Analysis: a new tool for investigating defects in nematic liquid crystals', Liquid Crystals, 26: 10, 1467 — 1478
To link to this Article: DOI: 10.1080/026782999203797
URL: http://dx.doi.org/10.1080/026782999203797

LIQUID CRYSTALS, 1999, VOL. 26, NO. 10, 1467–1478

Streamline Image Analysis: a new tool for investigating defects in nematic liquid crystals

A. SPARAVIGNA*†, A. SANNA‡, B. MONTRUCCHIO‡, A. STRIGAZZI†
†Dipartimento di Fisica and Istituto Nazionale di Fisica della Materia (INFM);
‡Dipartimento di Automatica e Informatica, Politecnico di Torino,
corso Duca degli Abruzzi 24, 10129 Torino, Italy

(*Received 16 March 1999; accepted 14 April 1999*)

A bidimensional investigation of the director field near defects normal to the symmetry plane in a nematic liquid crystal is here presented, based upon a new 'streamline' image processing of the data obtained by polarized light microscopy. With a visualization of vector field streamlines related to the actual director configuration, the disclination topological strength is revealed. The streamline visualization is also suitable for detecting smooth local variations of the director of field as functions of both space and time. Moreover, the orientation of the director field projection in the cell plane is determined with high sensitivity (~2%) and the possible presence of the out-of-plane escape of the director field is evaluated.

1. Introduction

An ordered medium can be regarded as a region described by a function assigning to every point an order parameter. Non-uniform media have an order parameter which varies continuously through the space except at isolated points, lines or surfaces, where the continuity is broken. These small definite regions of lower dimensionality are known as defects. Their consideration is involved in many fundamental physical systems: crystal dislocations, for instance, have a great influence on most physical properties [1]; thus they are an essential chapter in solid state physics. Point defects in semiconductors are also very important, due to their role in electrical and thermal transport [2].

Various approaches can be proposed for the study of defects. One is based on energetic considerations; it was the first to be introduced and is very important in relation to the existence and stability of defects in the crystals.

The deformation of liquid crystals (LCs) requires smaller energy than crystal distortion; as a consequence, defects are easily produced in LC samples. For instance, disclinations appear in the nematic phase, forming typical schlieren textures, which can be removed and destroyed by coalescence with a change of temperature. Such textures are fruitfully observed by optical microscopy: historically, it is from the optical investigation of defects that Friedel [3] deduced the symmetry of some liquid crystal phases.

*Author for correspondence; e-mail: amelia@ramses.polito.it

The energetic approach is nevertheless also the starting point for defect investigations in liquid crystals. For these systems, a topological classification [4–7] of defects, can be given as well. However, this procedure is used much more in the field of superconducting and magnetic materials, and in the case of two dimensional systems, when the bidimensionality plays an essential role.

As far as nematic liquid crystals are concerned, the mathematical description of the actual director configuration around disclinations was given in the frame of the continuum theory by Oseen [8] and Frank [9]; later, the subject was treated in greater detail by Nehring and Saupe [10]. Cladis and Kleman [11] and Meyer [12] showed that the singularity at the origin of defects in these planar models can be avoided by a non-singular continuous structure of lower energy: the director orientation 'escapes' in the third dimension. Observations and calculations in the cylindrical geometry reveal the strong influence of elastic parameters on the director deformation, with the appearance of a bistable behaviour of the material [13, 14]. The study of defects in nematic liquid crystals is therefore an intriguing problem both for their theoretical implications [15–17] and for their experimental investigation [18, 19], where the analysis of data obtained by optical microscopy using polarized light plays a fundamental role. New systems of data acquisition and image analysis, applied to microscopy, can greatly increase the sensitivity of observation, adding new skills for the identification of defects and textures [20, 21]. However, the data obtained from the experimental observations and the theoretical elaborations, showing

Journal of Liquid Crystals ISSN 0267-8292 print/ISSN 1366-5855 online
http://www.tandf.co.uk/JNLS/lct.htm
http://www.taylorandfrancis.com/JNLS/lct.htm

the director field in the textures under consideration, need to be graphically represented.

In fact, a graphical representation method can be used for two complementary purposes: the first is to visualize carefully the shape and the features of a streamline pattern coherent with a given collection of defects; the second is to infer from a given pattern texture recorded by camera the types and the distribution of the defects actually present in the sample. The main goal of our work is to clarify these two points and to achieve a generally effective method of visualization.

Recently a new method of visualization for vector fields has been proposed by Cabral and Leedom in the framework of computer science [22]: such an approach was called LIC, linear integral convolution. This procedure generates beautiful spread pictures of the field streamlines, resembling natural iron filing pattern in magnetic fields; however, no information on the local gradient of the streamlines is provided. We propose a new method of visualization of the nematic liquid crystal director field, suitable for defect investigation, but also highly effective in the case of a very general vector field.

In this paper a new image processing of the data observed by polarized light microscopy in the orthoscopic mode is presented: the method determines a bidimensional vector field characterizing the defect, that is the director field projection in the cell plane, and allows an effective visualization of the whole field streamlines over all the image under investigation. By analysing this pattern around the defect, the parameters of the disclinations can be immediately obtained. In fact, the quantitative measurement of the director alignment with respect to the polarizer axis, that is of the azimuthal angle, can be made with high sensitivity (azimuth sensitivity $\sim 2\%$). Furthermore, the director escape out of the cell plane can be evaluated, revealing whether or not a tilt angle is present.

2. Vector field description

In thin films sandwiched between two parallel glass plates, the macroscopic structure typical of the nematic phase (schlieren texture) can be observed between crossed polarizers (see figure 1). The black brushes originating from some points are due to 'line singularities', in our case perpendicular to the film, called disclinations. They are regions where the director is either parallel or perpendicular to the plane of polarization of the light incident on the sample. The position of those defect points is kept unchanged by turning the crossed polarizers with respect to the sample, whereas the brushes themselves rotate continuously. The sense of their rotation may be the same as that of the crossed polarizers (positive disclinations) or opposite (negative disclinations) [23].

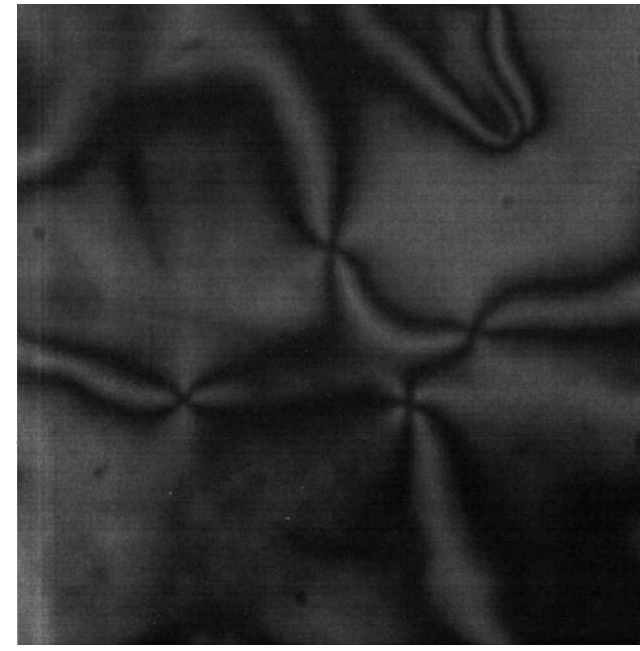

Figure 1. Schlieren texture in a nematic 5CB cell viewed between crossed polarizers. The points originating the black brushes are due to line singularities perpendicular to the cell plane. Disclinations of strength ± 1 are connected by brushes in the centre of the figure. The size of the figure is 200 μm × 200 μm.

The strength of a disclination, also called the topological charge, is defined by s = (number of brushes)/4: generally, we can observe in the nematic phase disclinations characterized by $s = +1/2, -1/2, +1$ and -1. Unlike spin systems, disclinations of topological strength $\pm 1/2$ are possible and stable in the nematic phase. A couple of neighbouring disclinations connected by brushes are of opposite sign. Considering a planar configuration of the director field $\mathbf{n}$ in the xy-plane (the z-axis being normal to the cell plates), achieved by a strong in-plane anchoring with a degenerated azimuthal easy direction, and assuming elastic isotropy ($K_{11} = K_{22} = K_{33} = K$), the cell free energy density F is coincident with the bulk one, and in principle is given by:

$$F = \frac{1}{2}K_{11}(\nabla \quad \mathbf{n})^2 + \frac{1}{2}K_{22}(\mathbf{n} \quad \nabla \times \mathbf{n})^2 + \frac{1}{2}K_{33}(\mathbf{n} \times \nabla \times \mathbf{n})^2 \tag{1}$$

but reduces to the simple form:

$$F = \frac{1}{2}K(\nabla \phi)^2 \tag{2}$$

calling ϕ the angle of the director field $\mathbf{n}$ with respect to the x-axis. Minimizing the free energy, the angle turns

out to be:

$$\phi = s \tan^{-1}\left(\frac{y}{x}\right) + c \qquad (3)$$

where c is an arbitrary constant, depending on the choice of the x-axis. The corresponding unit vector field is given by:

$$n_x = \cos\phi \quad n_y = \sin\phi \quad n_z = 0. \qquad (4)$$

For $|s| = 1$ defects, the singularity produced by the bidimensional model can be avoided by a non-singular continuous structure of lower energy where the director orientation escapes towards the z-dimension, then involving bend and splay. The component n_z is now different from zero, and so the problem is no longer bidimensional.

Regions where the orientation of the molecules changes abruptly can also be observed. These regions are indicated as inversion walls; they appear in nematic cells that are not too thin and have a surface treatment favouring planar alignment. Surface tilt and bulk inversion walls are bound to $|s| = 1/2$ lines [24].

In figure 2 the director field is shown in planar configuration around the defect points $s = 1$, $s = -1$ respectively, with $c = 0$ in both cases, see equation (3). In the figure we have introduced the angle Φ, formed by the director field with the polarizer axis; this angle will be used in the image processing analysis performed in this paper.

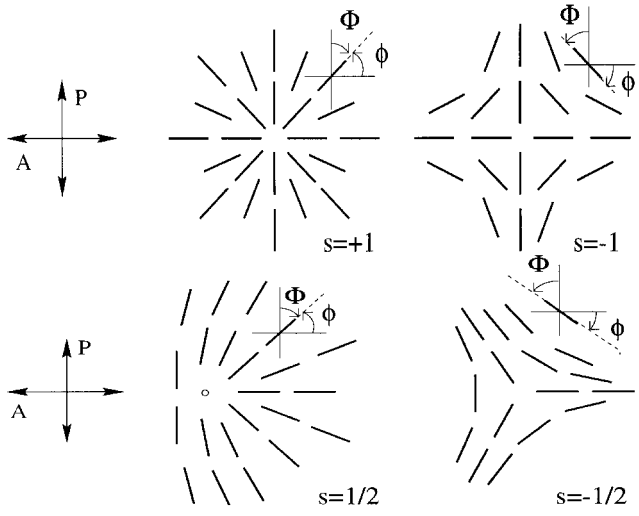

Figure 2. Local behaviour of the director of field for disclinations of strength + 1 and – 1 (upper part) and + 1/2 and – 1/2 (lower part). In the reference frame given by the crossed polarizer P and analyser A axis, the director is forming the angles Φ, ϕ respectively. Turning clockwise around the centre of the defect, Φ increases for positive defects and decreases for negative defects.

The gradient of Φ will be a vector field $\nabla\Phi$ turning clockwise around a defect with $s = 1$ and counterclockwise for $s = -1$, as can be easily seen from figure 2, moving along a circular path around the defect centre. Following this path clockwise, we realize that Φ is increasing for $s = +1$ and decreasing for $s = -1$. The same situation is shown by the defect of strength + 1/2 (clockwise) and – 1/2 (counterclockwise), as demonstrated in the lower part of figure 2. Note that $\nabla\Phi(x, y)$ is a local vector normal to the **n**-profile: in general $\nabla\Phi(x, y)$ is not normal to the radial straight line connecting the defect with the point $P(x, y)$.

The problem we want to solve here is the determination of the defect local strength and the azimuth Φ, by processing of the image obtained by microscopy observation of the region containing the defect. But before going into the details of the defect analysis, it is necessary to introduce the vector field representation which we have used for drawing the director **n** and the azimuth gradient field $\nabla\Phi$. Such a representation turns out to be essential for the determination of the sign of the defect strength.

3. Modelling the vector field

Starting from a given distribution of defects, the first step is to calculate the vector field. The second step is to give a useful visualization of its streamline pattern. For instance, if we consider only one defect point with strength ± 1, the director field can be easily calculated in the frame of the continuum theory, and the representation of the relevant streamlines can be obtained with common graphic software, giving a set of vectors on a convenient grid, as in figure 2.

Recently, Cabral and Leedom proposed a method called LIC (line integral convolution) for producing images and animations of field streamlines [22]. The LIC algorithm assumes as input data the vector field lying on a two dimensional Cartesian grid and a white noise map with the same size of grid. The white noise texture is a two dimensional image, each of its pixels possessing a grey tone, ranging from 0 to 255; the grey tones are randomly distributed in the image frame. The LIC produces as output image the input white noise map, which has been 'locally blurred' according to the vector field considered. In this way, a one-to-one correspondence is established between the grid cells in the vector field region and the pixels belonging to the input texture. As a consequence, the grey tone of an output pixel is obtained with a weighted average of the pixels of the white noise image along the local streamline of the vector field starting at the pixel (x, y) under consideration. The streamline allows us to identify a set of pixels on the input texture; then, the weighted average producing the output pixel intensity is determined by the 1D convolution [25]

of a filter kernel applied to the intensity of the pixels of the input texture along the local streamline, according to the formula:

$$P_{out}(x, y) = \sum_{p \in \tau} P_{in}(p) h(p) \qquad (5)$$

where p is the identification number of the arbitrary cell of the grid, τ is the set of cells along the local streamline within a set distance $\pm l/2$ from the starting point (x, y), l being the length where the convolution kernel $h(p)$ is different from zero, conveniently chosen according to the imposed resolution, and $P_{in}(p)$ is the pixel intensity of the input texture at the p-cell. Note that the convolution kernel $h(p)$ may be a simple rectangular filter with unit height and base l [22]. Let us stress that for other reasons the computation of the streamline actually can stop, i.e. when it is not possible to find a further next grid cell since either: (i) the streamline crosses the boundary of the region where the vector field is defined, or (ii) the magnitude of the field along the next grid cell vanishes.

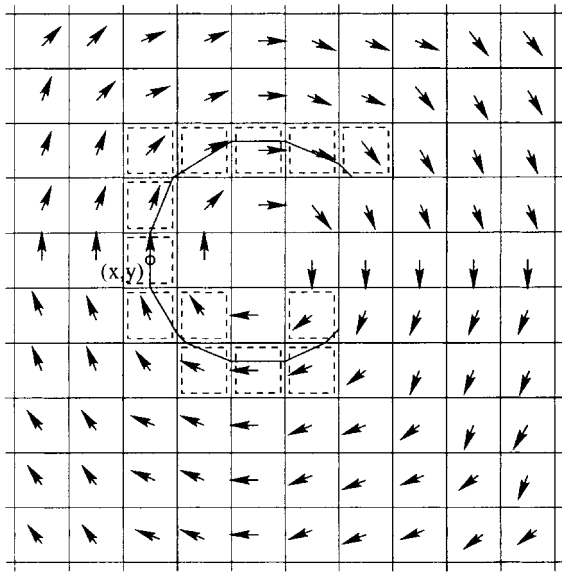

Figure 3. A 2D vector field showing the local streamline starting at the grid cell (x, y). The length set for the filter is 13 and the cells involved by the filter in the calculation are indicated by the broken lines.

An example of local streamline is shown in figure 3, where a vector field representing a bidimensional vortex is depicted. The streamline starts at the centre of the grid cell (x, y) and moves towards the 'positive' and 'negative' senses for a total length l (centred in the starting point: a path $l/2$ is described in both senses). The LIC application is shown in figure 4; where (a) represents the white noise texture (input image), and (b) shows the result of the LIC algorithm application (output image).

The LIC algorithm can be effectively employed in a large spectrum of topics [26], since it can be extended to visualize 3D flows [27–29]. Figure 5 shows the LIC representation of the director field around a couple of disclinations ($s = \pm 1$); the visualization sensitivity of the vector field is deeply enhanced by the operation of blurring.

Although the LIC algorithm allows an easy and fast representation of an arbitrary vector field, it is affected by two drawbacks: (i) it does not provide any information about the sense of the local orientation; (ii) it does not provide any direct information on the possible intensity variation of the vector field.

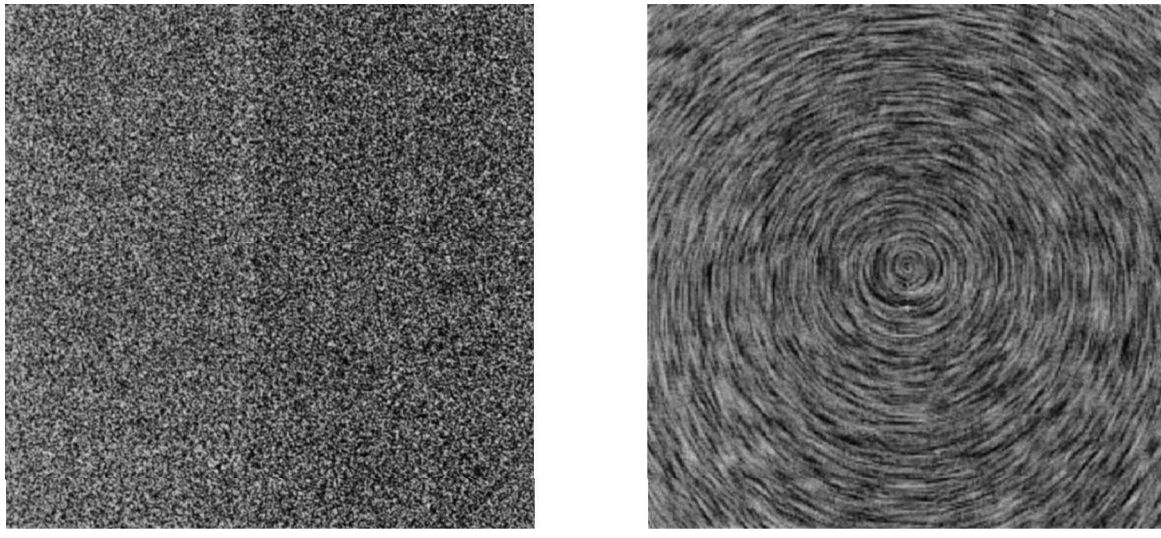

a b

Figure 4. White noise texture in (a) and the result of the LIC algorithm in (b) obtained by means of the vortex field of figure 3 applied to the noise texture.

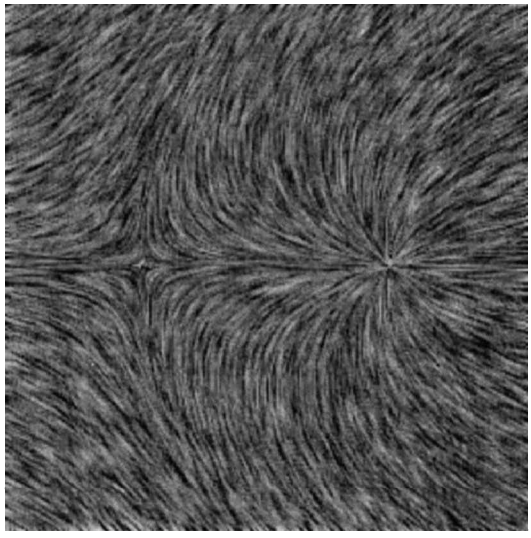

Figure 5. Application of the linear integral convolution (LIC) to the visualization of the director field in liquid crystals: field around a couple of disclinations of strength ± 1.

The sense of flow orientation could in principle be shown through animation; unfortunately, there are cases where a few still images are available. In order to solve these problems the advance software OLIC (Oriented LIC) was developed [30]. There are two main differences between LIC and OLIC: (i) LIC uses continuous noise textures, whereas OLIC utilizes only sparse textures; (ii) the convolution kernal in OLIC is asymmetric (ramp-like), instead of being a simple rectangular function. With an OLIC-like method a starting average grey tone is arbitrarily chosen and its intensity is varied linearly along the streamline according to the convolution filter. An example utilizing sparse textures and varying grey tone along the streamline (similar to OLIC) is shown in figure 6(*a*). There, a vortex with clockwise orientation is visualized, making the assumption that the local field is directed from the dark grey towards the white tone. Moreover, an enhanced version of OLIC, optimized with respect to the computing speed (FROLIC, Fast Rendering OLIC) was later developed [31]. Both procedures provide the sense of the local streamline orientation, but intrinsically give diffused information losses, due to the use of sparse textures.

A new approach [32] is presented in this paper, the application of which to the vortex is shown in figure 6(*b*). It overcomes the drawback of the LIC algorithm, which does not allow the identification of the flow sense, and the drawback of OLIC (FROLIC), which essentially produces information losses.

According to the method, the local streamline with arbitrary length l is computed for each grid cell of the vector field region. A first subset of the grid cells, chosen on the region of the vector field according to Sobol's distribution [33], is considered, such as that where the corresponding streamlines are centred on each cell belonging to this subset. Instead of computing a 1D convolution, the following procedure is performed to obtain the output texture. To the first pixel of these streamlines, a grey tone, chosen once for all the grid cells in a pseudo-random way, is assigned; the grey tone is then assumed to change along the streamline with an increasing rate proportional to the local amplitude of the vector field in the considered cell. This means that

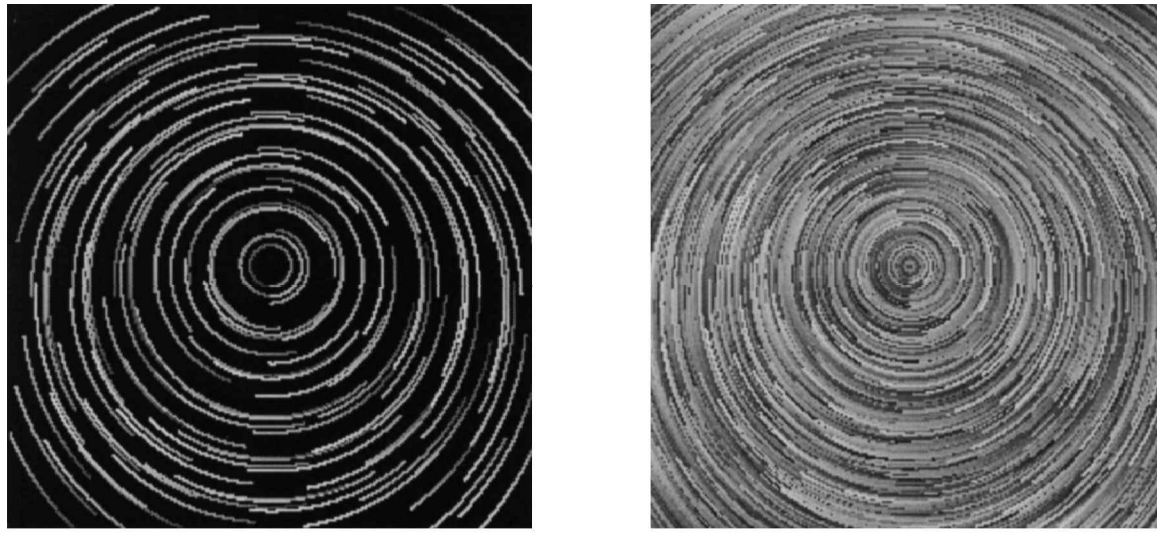

a b

Figure 6. The 2D vortex elaborated using sparse textures and varying grey tones along the streamlines (OLIC-like representation) is shown in (*a*). The same 2D vortex elaborated in (*b*) using dense and oriented streamlines, with the new procedure described in the text. The vortex is turning clockwise, assuming that the flow is going from the dark grey to white.

if the field is given by a unit vector (for instance, a nematic liquid crystal director), the grey tone just increases linearly.

Subsequently, the grid cells not belonging to the Sobol's distribution are treated in sequence, with the same previously stated procedure to assign grey tone values. In the case that two streamlines 'intersect', that is, if the cell pitch is too large for describing regions where the streamline concentration is high, the grey tone of the pixel in the output texture corresponding to the 'intersection' point is computed once when the first streamline is considered.

Figure 6 (*b*) shows the vortex treated by our method; the orientation is evident and no loss of detail occurs. In figure 7 the streamline representation with an OLIC-like method and with our method are compared, taking into account a region around a topological dipole ($\pm$ 1 disclination). Of course, in the presence of only one defect the definition of one orientation sense for the nematic director lines is without importance, due to the nematic symmetry ($\mathbf{n} = -\mathbf{n}$). But, if there are just two defects, the choice of a correlated orientation sense is very important, since it can discriminate between two dual patterns; in this case, it is possible to change from one configuration to the other only via an alignment transition [34].

4. Matching the experiment

Let us consider a nematic liquid crystal layer with planar configuration independent of the third coordinate z along the layer thickness. We deal with microscopic observation through crossed polarizers. Concerning the determination of the azimuth Φ of the director with respect to the polarizer axis, we follow the Born and Wolf [35] analysis for the calculation of the optic axis by means of the interference with crystal plates. Let us briefly summarize the method. A beam of linearly polarized light is normally incident on a sample consisting of a slab of thickness h: for instance, a nematic layer with director $\mathbf{n}(x, y)$ independent of z. On entering the slab, the beam is divided into two beams, with different ordinary and extraordinary propagation speeds, and with displacement electric vectors **D** vibrating in two mutually orthogonal directions normal to the propagation vector, i.e. parallel to the slab. They emerge from the slab with a certain phase difference δ. If the analyser is placed beyond the slab, then interference fringes of the beam components along the analyser polarization plane are observed. In the case of a planar nematic configuration, the optical axis lies in the plane of the layer plates and one beam is characterized by **D** vibrating in the direction of the optical axis; the other will have **D** perpendicular with respect to the previous beam.

In figure 8, the plane of the figure is parallel to the plate, that is to the cell walls. $\mathbf{D}'$ and $\mathbf{D}''$ represent the two mutually orthogonal displacement vectors of the refracted beams, and OP and OA are the polarization directions of the polarizer and analyser, respectively. Generally the polarizers are not crossed, but form an angle χ. $\mathbf{D}'$ and $\mathbf{D}''$ are either relevant to the ordinary $\mathbf{D}'' = \mathbf{D}_o$ and to the extraordinary $\mathbf{D}'' = \mathbf{D}_e$ beams, or vice versa; in the present analysis the two possibilities are indistinguishable. $\Phi(x, y)$ is the angle formed by the polarizer axis with $\mathbf{D}'$. The general intensity $I(x, y)$ of the light outgoing from the cell is dependent not only

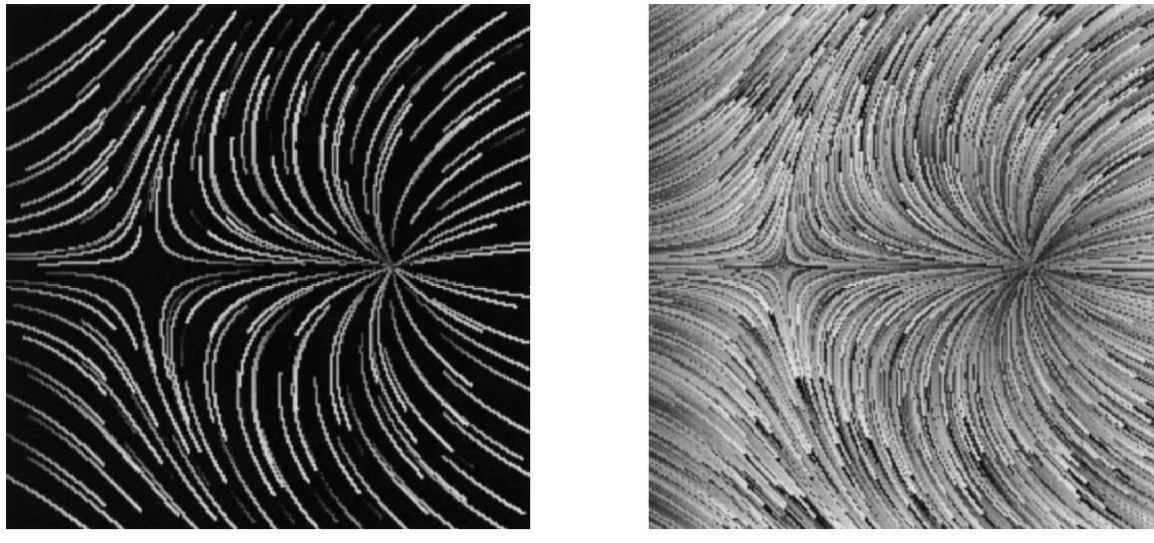

a b

Figure 7. OLIC representation in (*a*) compared with the streamline representation (*b*) introduced in the present paper for a $\pm$ 1 couple of disclinations. The streamline representation, due to the high density of the lines, avoids information losses.

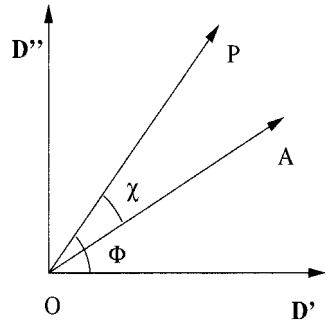

Figure 8. Reference frame constituted by the two vibration directions of the displacement electric fields **D**′, **D**″ in the birefringent material. **P** and A are the directions of the polarizer and analyser axes, forming the angle χ. Φ is the angle between the polarizer and one of the directions of the **D**-field.

on Φ and δ but also on χ:

$$I(x, y) = I_o[\cos^2 \chi - \sin 2\Phi \sin 2(\Phi - \chi) \sin^2(\delta/2)] \tag{6}$$

where I_o, constant for the whole cell, is the intensity of the incident light (if the reflected beam is negligible) and δ is the phase shift, which is given by:

$$\delta = \frac{2\pi}{\lambda}(n - n_o)h \tag{7}$$

where n_o is the ordinary and n is the effective refractive index, dependent on the tilt angle θ, which is the angle between **n** and the z-axis and λ is the light wavelength. In the case of the light transmitted by parallel polarizers, that is $\chi = 0$, the intensity is given by:

$$I_{\parallel}(x, y) = I_o[1 - \sin^2 2\Phi \sin^2(\delta/2)]. \tag{8}$$

In the case of the light transmitted by orthogonal polarizes, that is $\chi = \pi/2$:

$$I_{\perp}(x, y) = I_o \sin^2 2\Phi \sin^2(\delta/2). \tag{9}$$

Then:

$$I_o = I_{\parallel} + I_{\perp} \tag{10}$$

which is Malus's law. Hence the local azimuth Φ is given by:

$$\Phi(x, y) = \frac{1}{2} \tan^{-1}\left[\frac{I_{\perp} \sin 2\chi}{I - (I_o)\cos^2 \chi + I_{\perp} \cos 2\chi}\right]. \tag{11}$$

Note that for better elaboration of the optical data the local 'point' $P(x, y)$ is considered as an average of a set of neighbouring pixels corresponding to $\lambda/2$. Equation (11) is valid for a distortion independent of z; however, a more complex analysis is necessary for a configuration involving a tilt angle dependent on z [36]. Equation (11) may nevertheless be used if an effective orientation, averaged on the cell thickness is assumed; Φ is then the effective angle formed by the projection of the director **n** on the cell plane.

To obtain Φ, in the simplest possible approach, three images giving I, $I_{\parallel}$, $I_{\perp}$ of the liquid crystal cell are necessary. The cell was a common sandwich type, with a gap of 23 μm ensured by mylar spacers. The inner surfaces of the cell glass plates were simply rubbed in order to favour a unidirectional planar alignment in one privileged direction. The nematic liquid crystal, 5CB, was introduced into the cell by capillarity in the isotropic phase. All the measurements were performed at room temperature. The optical investigation was carried out using a Leitz polarizing microscope. A JVC color CCD camera with fixed shutter was used for recording the observations and a frame grabber was used to digitize the images. An interference filter produced monochromatic (green) light with wavelength 546 nm.

The defects we analyse are shown in figure 9. The figure shows the images of defects $s = \pm 1$ with parallel polarizers ($I_{\parallel}$), with polarizer and analyser forming 40°

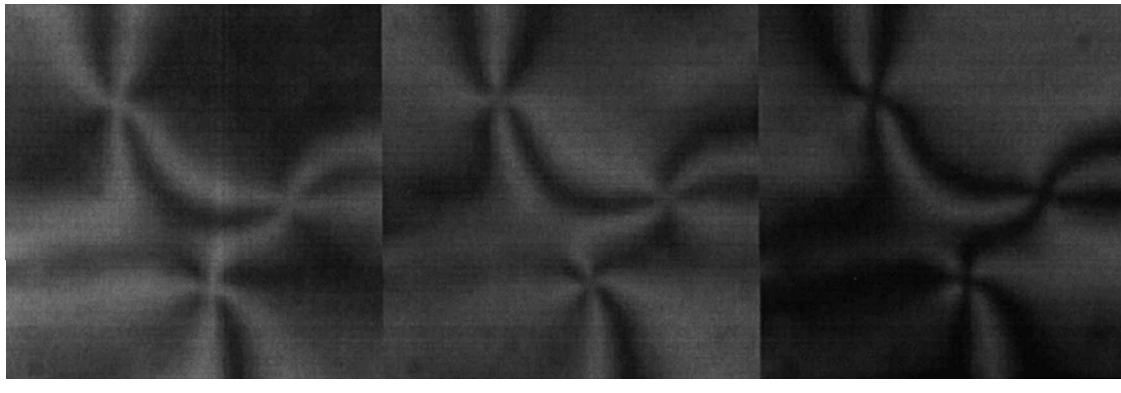

Figure 9. Three images are necessary for the defect investigation: the images show the central part in figure 1 and are obtained with parallel polarizers, with polarizer and analyser forming 40° and for crossed polarizers (from left to right). In the measurement, the cell remains in a fixed position, only the analyser being turned. Each image size is 100 μm × 100 μm.

(I) and for crossed polarizers ($I_\perp$). The three images are converted into three corresponding bitmap files, in which to each pixel of the image there corresponds a grey tone (ranging from 0 to 255) proportional to the intensity of the light. Let us note that the data must be corrected by the background field obtained by recording the signal of the camera with crossed polarizers and without the liquid crystal cell. Calculating the angle Φ according to equation (11), it is possible to see immediately the sign of the defect strength by means of the visualization of $\nabla\Phi$ as discussed in §2. The elaboration of the experimental data made by means of the visualization procedure discussed in §3, is shown in figure 10, where we can see immediately whether $\nabla\Phi$ is clockwise or counterclockwise, that is of $+1$ or -1 strength, by the turning streamlines. The regions where the angle Φ is constant and then $\nabla\Phi = 0$ turn out to be hairy (or entangled without apparent order).

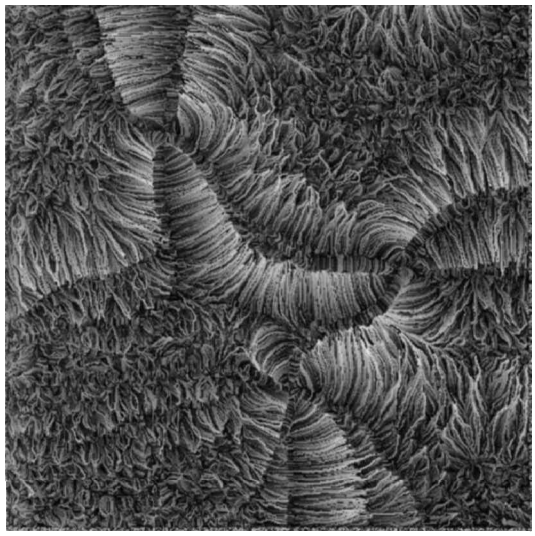

Figure 10. The field $\nabla\Phi$ of the disclinations of figure 9 viewed by the streamline image processing proposed in this paper: let us note the rolling of the field clockwise and counterclockwise around positive and negative strength disclinations. Points with different charges are connected by the streamlines.

It is also possible to check the behaviour of the director field projection, coming directly from the value of the angle Φ, and to produce an image visualizing this field from experimental data, without simulating it by means of any theoretical models.

Let us stress that the proposed method of analysis allows us to characterize the distortion features without turning the sample: it is only necessary to turn the analyser with respect to the polarizer.

To check the procedure, let us analyse in much more detail the field around the defects, zooming in on a positive and a negative defect. Starting from the positive defect, let us show the gradient field $\nabla\Phi$ and the director field projection, in figure 11 (*a*) and 11 (*b*), respectively. The frame of each figure is subdivided into four regions. In two of these regions marked A and A′ in figure 11 (*b*), it is possible to recognize the same behaviour of the director field for the disclination of strength $+1$, shown in figure 2; whereas in the other two, marked B and B′,

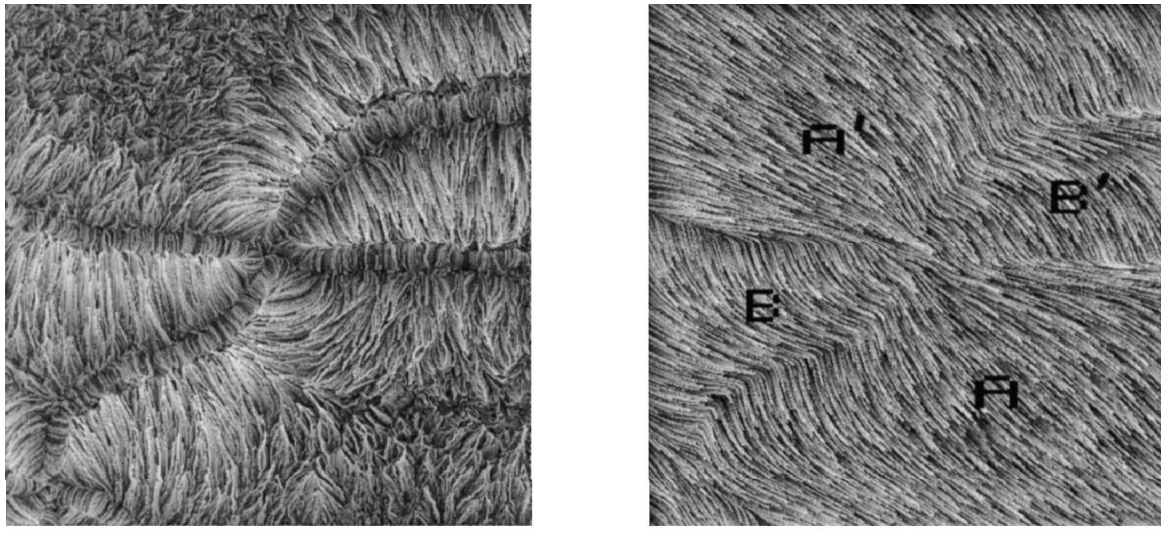

a b

Figure 11. Details of the $\nabla\Phi$ field (*a*) and of the projection of the director field in the cell plane (*b*), around the positive disclination in figure 10. Concerning the projection of the director field, the region around the defect is subdivided into four parts: the typical radial behaviour of the field (shown in figure 2) is easily recognizable in two of the regions (AA′). In the other two (B, B′), the calculation shows the streamlines of the perpendicular to the **n**-projection. The size of each image is 40 μm × 40 μm.

the calculations of Φ by equation (11) exhibit the perpendicular behaviour to the projection of the director field. This is the limit of our approach—the inability to distinguish the direction **D′** from **D″**.

The pattern shown in figure 11 (*b*), composed of two regions with radial streamlines and two with circular ones, is typical of defects with strength $s = +1$. In figure 11 we have used for both fields our streamline representation. In fact it is strictly necessary only for the $\nabla\Phi$ field, and not for the projection of the director field, but it proves to be much more effective for the visualization in comparison with LIC and OLIC: the orientation of the streamlines helps the observer to follow the pattern in the image. Let us stress that in figures 11 (*a*) and 11 (*b*), elaborations of experimental data are presented, independently of any particular modelling of the director field near the defect.

To investigate the quantitative behaviour of the angle Φ, let us fix a polar axis parallel to the horizontal direction of the image (see figure 12), with the origin in the defect and oriented towards the right. A polar angle Ω is introduced: turning Ω through an angle 2π, performing in this way a circular clockwise path with a fixed radius around the centre of the defect, the angle Φ obtained by the experimental investigation is calculated. The result of the elaboration is shown in figure 13, for a radius of 15 μm: the angle is growing in each of the four regions A, A′, B and B′ with a value of the angle Φ obtained by equation (11) included in the range from 0 to $\pi/2$.

As previously said, this limitation provides different directions of the in-plane **n**-projection field in the AA′ and the BB′ regions. In figure 14, the same results as figure 13 are reported, corrected with the $\pi/2$ multiples.

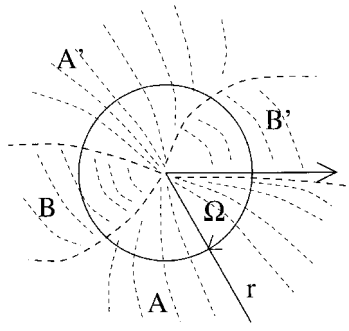

Figure 12. Polar axis and polar angle Ω used for the analysis of the behaviour of the angle Φ.

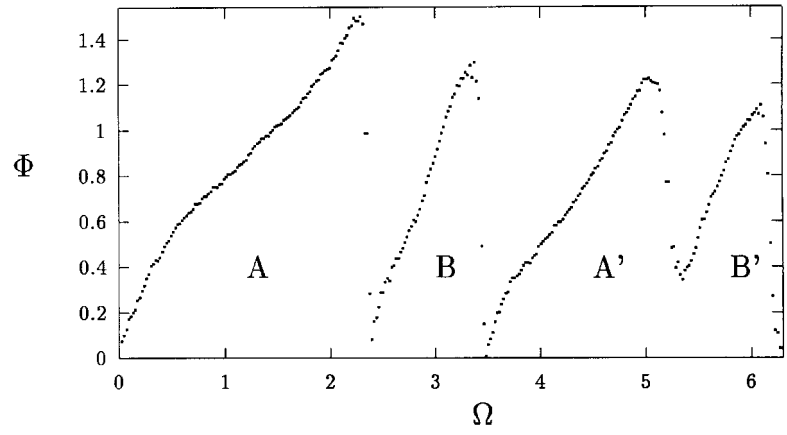

Figure 13. Angle Φ (in radians) around the defect of +1 strength shown in figure 11 as a function of the polar angle Ω (in radians) for a circular clockwise path of radius 15 μm around the defect. A, A′ and B, B′ mark the regions shown in figure 11 (*b*).

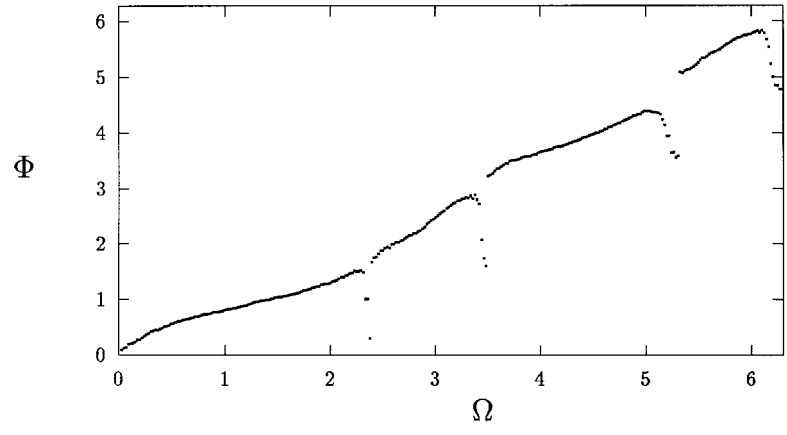

Figure 14. The same as in figure 13, with the value of the angle Φ (in rad) corrected by the $\pi/2$ multiples. Following a circular pattern around the defect, the non-perfect radiality of the projection of the director field produces discontinuities in the angle Φ.

Since the projection field is not perfectly radial, discontinuities in the angle Φ can be observed in figure 14: they are artifacts, due to the necessity of following a circular path around the defect.

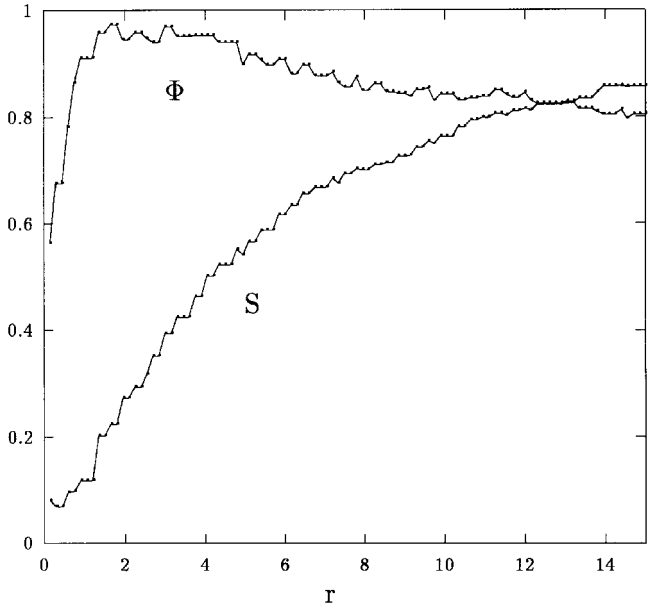

Figure 15. Behaviour of the angle Φ (in radians) and of the parameter $S = \sin^2(\delta/2)$ as a function of the radial distance r from the defect (microns), for a fixed polar angle Ω ($\Omega = 60°$). Note that the parameter S depends on the difference between the ordinary refractive index n_o and the effective refractive index n, which is tilt dependent.

After choosing a particular radial direction, far from those subjected to the discontinuities, it is possible to investigate the azimuth Φ as a function of the radial distance r from the defect. Moreover, as one can see from equation (9), when the angle is obtained, the parameter

$$S = \sin^2(\delta/2) \tag{12}$$

can be calculated. Let us remember that δ is dependent on the difference between the ordinary and the effective refractive indices. The effective refractive index n is dependent on the tilt angle θ of the director field, the ordinary index n_o remaining unchanged. According to experimental data [37] for refractive indexes n_o and n_e of 5CB, S turns out to be 0.939, if the nematic possesses a planar configuration. In figure 15, Φ and S are reported as a function of r for $\Omega = 60°$: S reveals that a tilt is present and is not negligible for r less than 12 μm.

At the same time, the azimuth Φ goes at the origin to a value of 0.65–0.7 rad, corresponding to 38–40°: this it is not surprising, if we suppose that in the central part of the defect the molecules of the nematic are perpendicular to the cell plane. In this case the liquid crystal behaves like an isotropic system, and the calculation of Φ gives the angle χ between polarizer and analyser.

In figure 16 the $\nabla\Phi$ and Φ profiles of the upper negative disclination are investigated; also in this case, the director field that is represented in the two regions A, A′ of the image corresponds to the theoretical **n**-lines shown in figure 2. In the other two regions B, B′, there

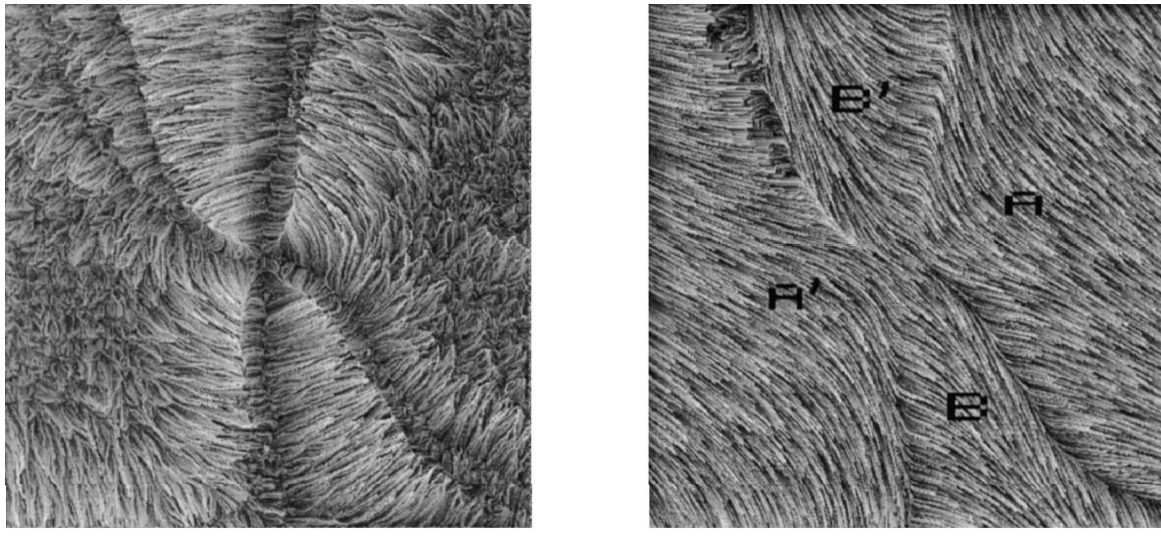

a b

Figure 16. Details of the $\nabla\Phi$ field (*a*) and of the projection of the director field in the cell plane (*b*), around the upper negative disclination of figure 10. As in the case of the positive defect, the region around the defect is subdivided into four parts: the typical behaviour of the field around an $s = -1$ defect (shown in figure 2) is easily recognizable in two of the regions (AA′). In the other two (B, B′), the calculation makes evident the distribution of the streamlines perpendicular to the **n**-projection. The size of each image is 40 μm × 40 μm.

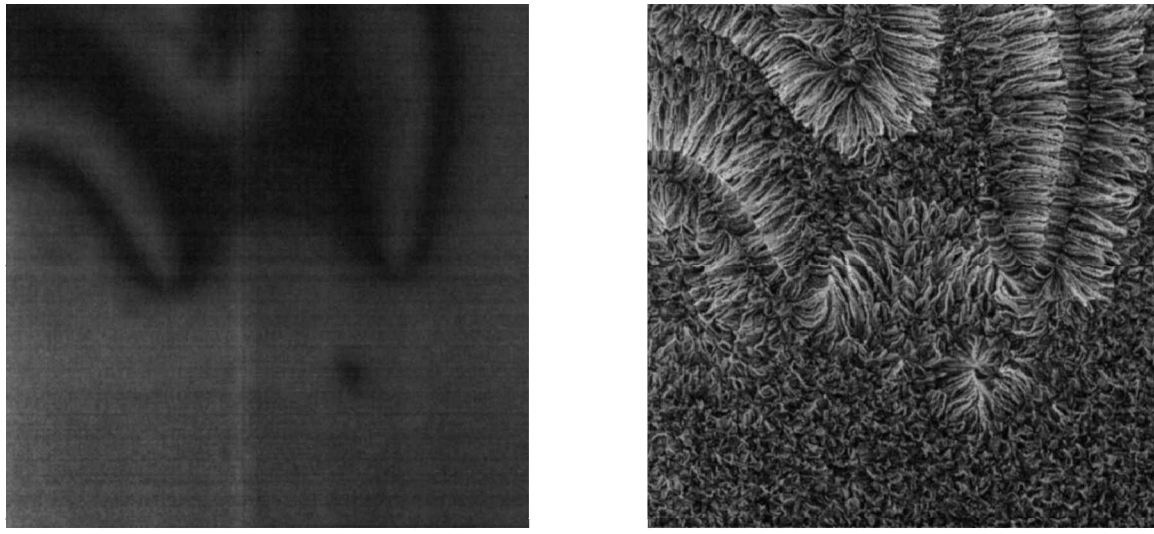

Figure 17. Disclinations of ± 1/2 strength viewed between crossed polarizers in (*a*) and the elaboration of the $\nabla\Phi$ field (*b*), showing the sign of the topological charges. The size is 80 μm × 80 μm.

is simply shown the perpendicular to the projection of the director field. The pattern shown in these four regions is typical of defects with strength $s = -1$ and different from that of the defects with $s = +1$: the different patterns of the projection field around the defect then correspond to defects with different strength.

Let us now discuss the behaviour of the projection of the director field near the defects of strength 1/2. Figure 17 (*a*) shows ± 1/2 defects between crossed polarizers; figure 17 (*b*) however is the elaboration of $\nabla\Phi$, by means of our visualization procedure, that shows the positive (on the right) and the negative (on the left) defect. In the case of the + 1/2 disclination, let us analyse the behaviour of the angle Φ and of the parameter S as functions of the radial distance r from the positive defect. We can see from figure 18 that no essential variation of S is present on approaching the defect, confirming the absence of axial escape for a defect of 1/2 strength [6].

Comments must be made about the accuracy and the sensitivity in the evaluation of the angle Φ by means of the image processing. In fact, the accuracy of the measurement lies in the recording of the images coming from the CCD camera and from the data digitization. After subtraction of the background field, the histogram of each image must be checked to see if this procedure reaches a cut-off in the pixel distribution [25]. Only in the negative case are the images reliable and able to be properly analysed.

To determine the sensitivity of the method, we evaluated the mean value Φ_m of the angle Φ over single squares of the image, centred in each pixel of the image frame, with size coincident with one half of the wavelength. Subsequently, the absolute value of the deviation

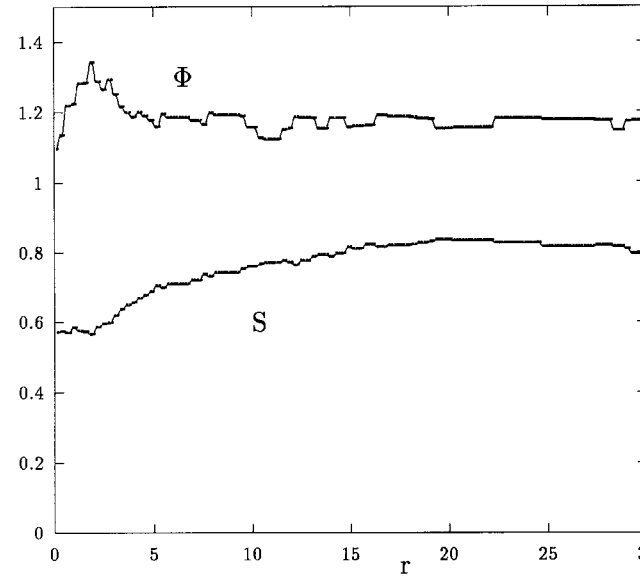

Figure 18. Behaviour of the angle Φ (in radians) and of the parameter $S = \sin^2(\delta/2)$ as a function of the radial distance r from the + 1/2 defect (microns), for a fixed polar angle Ω ($\Omega = 90°$). No essential variation of S is present on approaching the defect.

$\Delta\Phi$ from the average Φ_m in each square was computed. After analysing all the image pixels we assumed the biggest value of the ratio $|\Delta\Phi|/\Phi_m$ as the sensitivity of the measurement, choosing the less favourable event. The estimate of the sensitivity proves to be about 2%. In the calculation, we neglected pixels having the corresponding square crossing a discontinuity of the azimuth Φ.

5. Conclusion and remarks

A new graphical representation method is proposed in this paper: it has been essentially used to infer from a given pattern texture recorded by a camera the types and the distribution of the defects actually present in a nematic sample. However, it can be generally used to visualize the shape and features of the director configuration. Good visualization means not only the correct representation, but also indications able to give a synthesis and to suggest the physical properties of the configuration considered.

In fact, we needed to introduce a new vector field visualization, the streamline one, not only to describe the local behaviour of the field, but also to demonstrate the global feature of the director profile, indicating directly the topological charge of the possible defects.

Moreover, the new analysis of the data obtained by optical microscopy shows graphically the distribution of the local angle gradient $\nabla\Phi$ and allows the determination, with high sensitivity, of the azimuth Φ, i.e. of the angle formed by the projection of the director with the polarizer axis. Axial escape is also revealed in the case of disclinations of strength equal to ± 1, and is found to be negligible for disclinations equal to $\pm 1/2$.

References

[1] Nabarro, F. R. N., 1985, *Dislocations in Solids* (The Netherlands: VSP).

[2] Yu, P. Y., and Cardona, M., 1996, *Fundamentals of Semiconductors* (Berlin: Springer-Verlag).

[3] Friedel, G., 1922, *Ann. Phys. (Paris)*, **18,** 273.

[4] Michel, L., 1980, *Rev. mod. Phys.*, **52,** 617.

[5] Mermin, N. D., 1979, *Rev. mod. Phys.*, **51,** 591.

[6] Kléman, M., 1977, *Points. Lignes. Parois.* (Orsay: Les Editions de Physique).

[7] Boltenhagen, Ph., Lavrentovich, O. D., and Kléman, M., 1992, *Phys. Rev. A*, **46,** R1743.

[8] Oseen, G. W., 1933, *Trans. Faraday Soc.*, **29,** 883.

[9] Frank, F. C., 1958, *Discuss. Faraday Soc.*, **25,** 19.

[10] Nehring, J., and Saupe, A., 1972, *J. chem. Soc. Faraday Trans. II*, **68,** 1.

[11] Cladis, P. E., and Kléman, M., 1972, *J. Physique*, **33,** 591.

[12] Meyer, R. B., 1973, *Phil. Mag.*, **27,** 405.

[13] Palffy-Muhoray, P., Sparavigna, A., and Strigazzi, A., 1993, *Liq. Cryst.*, **14,** 1143.

[14] Sparavigna, A., Palffy-Muhoray, P., and Strigazzi, A., 1993, *Int. J. mod. Phys. B*, **7,** 1143.

[15] Arodz, H., and Stelzer, J., 1998, *Phys. Rev. E*, **57,** 3007.

[16] Bogdanov, A. N., and Shestakov, A. A., 1998, *J. exp. theor. Phys.*, **87,** 911.

[17] Sonnet, A. M., and Virga, E. G., 1997, *Phys. Rev. E*, **56,** 6834.

[18] Crawford, G. P., Allender, D. W., and Doane, J. W., 1992, *Phys. Rev. A*, **45,** 8693.

[19] Ondris-Crawford, R. J., Crawford, G. P., Zûmer, S., and Doane, J. W., 1993, *Phys. Rev. Lett.*, **70,** 194.

[20] Montrucchio, B., Sparavigna, A., and Strigazzi, A., 1998, *Liq. Cryst.*, **24,** 841.

[21] Montrucchio, B., Sparavigna, A., Torgova, S. I., and Strigazzi, A., 1998, *Liq. Cryst.*, **25,** 613.

[22] Cabral, B., and Leedom, L., 1993, *Imaging Vector Fields Using Line Integral Convolution*, ACM Computer Graphics (Proceedings Siggraph), p. 263.

[23] Chandrasekar, S., 1992, *Liquid Crystals* (Cambridge: Cambridge University Press).

[24] Demus, D., and Richter, L., 1978, *Textures of Liquid Crystals* (Leipzig: VEB Deutscher Verlag für Grundstoffindustrie).

[25] Jähne, B., 1993, *Digital Image Processing: Concepts, Algorithms, and Scientific Applications* (Springer-Verlag).

[26] Shen, H.-W., 1997, *Comput. Phys.*, **11,** 474.

[27] Forsell, L. K., and Cohen, S. D., 1995, *IEEE Transaction on Visualization and Computer Graphics*, **1,** 133.

[28] Interrante, V., and Grosch, C., 1998, *IEEE Computer Graphics & Applications*, **18,** 49.

[29] Shen, H.-W., and Kao, L. D., 1988, *IEEE Transaction on Visualization and Computer Graphics*, **4,** 98.

[30] Wegenkittl, R., and Gröller, E., Purgathofer, W., 1997, *Animating Flowfields: Rendering of Oriented Line Integral Convolution*, in Proceedings of Computer Animation '97, June 1997, Geneva, Switzerland, p. 15.

[31] Wegenkittl, R., and Gröller, E., 1997, *Fast Oriented Line Integral Convolution for Vector Field Visualization via the Internet*, in Proceedings of IEEE Visualization '97, p. 309.

[32] Montuschi, P., Montrucchio, B., Sanna, A., and Sparavigna, A., private communication.

[33] Sobol, I., 1967, *USSR Comput. Math. math. Phys.*, **7,** 86. Sobol's distribution is a pseudo-random bidimensional probability density.

[34] Komitov, L., Lagerwall, S. T., Sparavigna, A., Stebler, B., and Strigazzi, A., 1992, *Mol. Cryst. liq. Cryst.*, **223,** 197.

[35] Born, M., and Wolf, E., 1997, *Principles of Optics* (Cambridge: Cambridge University Press).

[36] Jones, R. C., 1942, *J. opt. Soc. Am.*, **32,** 486.

[37] Bahadur, B. (editor), 1990, *Liquid Crystals, Applications and Uses* (Singapore: World Scientific Pub).